

Insights into the electric double-layer capacitance of two-dimensional electrically conductive metal-organic frameworks

Jamie W. Gittins,¹ Chloe J. Balhatchet,² Yuan Chen,^{1, 2, 3} Cheng Liu,⁴ David G. Madden,⁵ Sylvia Britto,⁶ Matthias J. Golomb,⁷ Aron Walsh,⁷ David Fairen-Jimenez,⁵ Siân E. Dutton,⁴ and Alexander C. Forse^{1*}

¹Yusuf Hamied Department of Chemistry, University of Cambridge, Lensfield Road, Cambridge CB2 1EW, U.K.

²Department of Chemistry, Imperial College London, Exhibition Road, London SW7 2AZ, U.K.

³The Faraday Institution, Quad One, Harwell Science and Innovation Campus, Didcot OX11 0RA, U.K.

⁴Cavendish Laboratory, University of Cambridge, JJ Thomson Avenue, Cambridge CB3 0HE, U.K.

⁵Adsorption & Advanced Materials Laboratory (A²ML), Department of Chemical Engineering & Biotechnology, University of Cambridge, Philippa Fawcett Drive, Cambridge CB3 0AS, U.K.

⁶Diamond Light Source, Harwell Science and Innovation Campus, Didcot OX11 0DE, U.K.

⁷Department of Materials, Imperial College London, Exhibition Road, London SW7 2AZ, U.K.

Abstract

Two-dimensional electrically conductive metal-organic frameworks (MOFs) have emerged as promising model electrodes for use in electric double-layer capacitors (EDLCs). However, a number of fundamental questions about the behaviour of this class of materials in EDLCs remain unanswered, including the effect of the identity of the metal node and organic linker molecule on capacitive performance and the limitations of current conductive MOFs in these devices relative to traditional activated carbon electrode materials. Herein, we address both these questions via a detailed study of the capacitive performance of the framework $\text{Cu}_3(\text{HHTTP})_2$ (HHTTP = 2,3,6,7,10,11-hexahydroxytriphenylene) with an acetonitrile-based electrolyte, finding a specific capacitance of 110 – 114 F g⁻¹ at current densities of 0.04 – 0.05 A g⁻¹ and a modest rate capability. By, directly comparing its performance with the previously reported analogue, $\text{Ni}_3(\text{HITP})_2$ (HITP = 2,3,6,7,10,11-hexaminoxytriphenylene), we illustrate that capacitive performance is largely independent of the identity of the metal node and organic linker molecule in these nearly isostructural MOFs. Importantly, this result suggests that EDLC performance in general is uniquely defined by the 3D structure of the electrodes and the electrolyte, a significant finding not demonstrated using traditional electrode materials. Finally, we probe the limitations of $\text{Cu}_3(\text{HHTTP})_2$ in EDLCs, finding a limited cell voltage window of 1.3 V and only a modest capacitance retention of 81 % over 30,000 cycles, both significantly lower than state-of-the-art porous carbons. These important insights will aid the design of future conductive MOFs with greater EDLC performances.

36 Introduction

37 The improvement of energy storage devices is critical for society to meet increasing energy
38 demands and allow for the integration of renewable energy sources into energy grids.¹⁻³ Electric
39 double-layer capacitors (EDLCs), a sub-set of supercapacitors, are among the most promising
40 energy storage devices due to their high power densities, which result in rapid
41 charging/discharging times, and excellent cyclability. As a result, EDLCs have potential uses
42 in applications where other energy storage devices are not suitable e.g., in heavy electrical
43 vehicles, storing energy rapidly from intermittent renewable energy sources.³⁻⁶ However, state-
44 of-the-art industrial EDLCs have low energy densities, which impedes their widespread use.
45 Potential performance gains could be achieved by optimizing the structure of the electrodes and
46 this may facilitate the use of supercapacitors more widely. Structure-property investigations to
47 determine how performance varies with electrode structure are challenging with traditional EDLCs
48 as many use porous carbons as the electrode material.^{7,8} These tend to have poorly defined
49 structures that are difficult to characterize, leading to structure-property investigations with
50 conflicting results.⁹⁻¹⁴

51 Recently, significant work has been done to develop new electrode materials for EDLCs with
52 well-defined structures. One such class of materials is two-dimensional electrically conductive
53 metal-organic frameworks (MOFs).¹⁵ These materials are generally formed from the square
54 planar coordination of late transition metal M^{2+} nodes by planar conjugated organic linker
55 molecules to form π -d conjugated 2D sheets. These sheets then stack, normally in an eclipsed
56 or near-eclipsed fashion, to form an extended 3D honeycomb structure, creating pores that run
57 through the material (**Fig. 1a**).^{16,17} Conductive MOFs are promising for use as EDLC electrodes
58 as they have high intrinsic conductivities (up to 2500 S cm^{-1}) and porosities (surface areas of 500
59 – ca. $1400 \text{ m}^2 \text{ g}^{-1}$).¹⁸⁻²⁰ Furthermore, the tuneable crystalline structures of conductive MOFs make
60 them interesting materials for use as model electrodes in structure-property investigations.
61 Despite this promise and much exploration as electrode materials in other energy storage
62 devices, including batteries, few conductive MOFs have been explored in EDLCs, particularly with
63 more commercially relevant organic electrolytes.²¹⁻²⁶ However, a key example is $\text{Ni}_3(\text{HITP})_2$ (HITP
64 = 2,3,6,7,10,11-hexaiminotriphenylene), which demonstrated high capacitive behaviour ($111 -$
65 116 F g^{-1} at 0.05 A g^{-1}) as the sole electrode material in a symmetric EDLC with $1 \text{ M NEt}_4\text{BF}_4$ in
66 acetonitrile electrolyte.²⁷ The closely related framework $\text{Cu}_3(\text{HHTP})_2$ (HHTP = 2,3,6,7,10,11-
67 hexahydroxytriphenylene) was also explored in EDLCs with aqueous and solid-state gel
68 electrolytes, and while nanowire arrays (NWAs) of this MOF exhibited good capacitive

69 performance, electrodes made using $\text{Cu}_3(\text{HHTP})_2$ powder exhibited relatively poor capacitive
70 behaviour.^{28,29} Here, we build on these studies and present a detailed analysis of the electric
71 double-layer capacitance of $\text{Cu}_3(\text{HHTP})_2$ in EDLCs with an organic electrolyte. Using a recently
72 published synthesis, as well as traditional electrode film processing methods, we find that
73 $\text{Cu}_3(\text{HHTP})_2$ exhibits very similar performance to $\text{Ni}_3(\text{HITP})_2$ in terms of capacitance, rate
74 capability, and cycling stability, suggesting that EDLC performance is independent of the identity
75 of the metal node and organic linker in these almost isostructural frameworks.³⁰

76

77 **Results & Discussion**

78 $\text{Cu}_3(\text{HHTP})_2$ was synthesized by modifying a recently published procedure (see SI Methods).³⁰
79 The identity and structure of the MOF were confirmed via powder X-ray diffraction (PXRD), with
80 the experimentally obtained PXRD pattern comparing well to those simulated using hexagonal
81 eclipsed and monoclinic near-eclipsed crystal structures of $\text{Cu}_3(\text{HHTP})_2$, both polytypes of the C-
82 centred monoclinic structure due to the sub-supergroup relation but with variations in the stacking
83 of the 2D layers (**Fig. 1a, b**; SI Figs. S1, S2; Table S1). However, the quality of the PXRD data is
84 insufficient for Rietveld refinement and therefore insufficient to distinguish between the models
85 with any degree of certainty. To gain further information on the structure of the synthesized
86 $\text{Cu}_3(\text{HHTP})_2$, Cu K-edge X-ray absorption near edge structure (XANES) was performed on a
87 powdered sample, and the obtained spectrum compared to those simulated using the two crystal
88 structures described above (**Fig. 1c**). The results are supportive of previous work indicating that
89 $\text{Cu}_3(\text{HHTP})_2$ may have a near-eclipsed crystal structure, with a constant stacking shift of the 2D
90 layers, as opposed to the closely related eclipsed structure exhibited by $\text{Ni}_3(\text{HITP})_2$.³¹ Cu K-edge
91 XANES was also used to probe the Cu oxidation states present in the MOF. This confirmed that
92 Cu(II) is the dominant Cu oxidation state in the as-synthesized MOF with no clear evidence for
93 the presence of Cu(I) (SI Fig. S3). This result helps to clarify debate in the literature on the Cu
94 oxidation states in the framework, with some previous XANES and X-ray photoelectron
95 spectroscopy (XPS) investigations indicating the presence of Cu(I) in the MOF synthesized using
96 different methods.^{32,33} We subsequently evaluated the porosity and Brunauer, Emmett and Teller
97 (BET) areas using 77 K N_2 adsorption isotherms. A maximum BET area of $794 \text{ m}^2 \text{ g}^{-1}$ was
98 calculated using Rouquerol's updated criteria implemented in BETSI (SI Fig. S4).³⁴ This is the
99 highest reported BET area for this material, comparable to the BET area of $\text{Ni}_3(\text{HITP})_2$, and

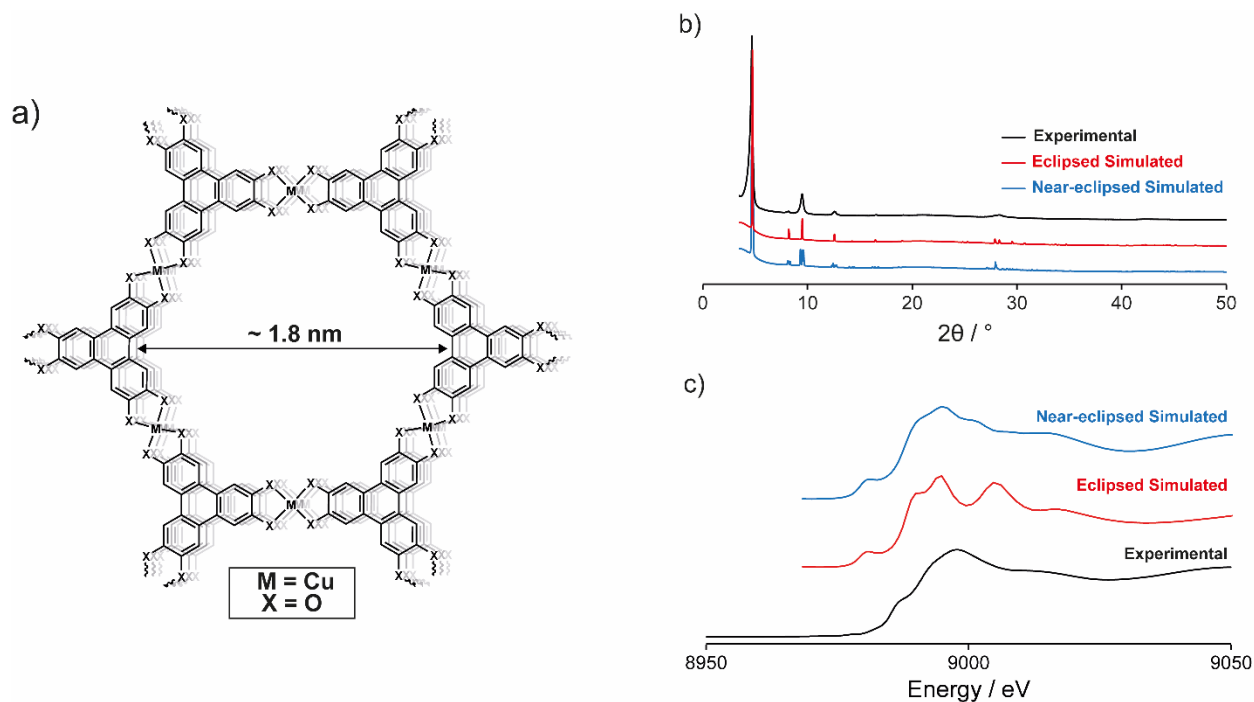


Fig. 1 (a) Schematic demonstrating the general structure of hexasubstituted triphenylene-based conductive MOFs. The π -d conjugated 2D sheets stack to form an extended 3D honeycomb structure. This creates pores/channels that run through the material, with a pore size of 1.8 nm as calculated from the simulated structure of $\text{Cu}_3(\text{HHTP})_2$. (b) The experimental PXRD pattern of $\text{Cu}_3(\text{HHTP})_2$ compares well to simulated PXRD patterns of $\text{Cu}_3(\text{HHTP})_2$ with both eclipsed and near-eclipsed crystal structure. (c) Experimentally obtained Cu K-edge XANES of $\text{Cu}_3(\text{HHTP})_2$ shows better agreement with the simulated XANES of $\text{Cu}_3(\text{HHTP})_2$ with a near-eclipsed crystal structure.

100 confirms permanent porosity, a key requirement for double-layer capacitance.^{27,35} Elemental
 101 analysis confirmed that the as-synthesized $\text{Cu}_3(\text{HHTP})_2$ has approximately the correct
 102 stoichiometric ratio of Cu and HHTP, although a small amount of a N-containing impurity was also
 103 present, most likely due to the use of ammonia as a modulator in the synthesis (see SI Methods).

104 Having characterized the crystalline structure and porosity of $\text{Cu}_3(\text{HHTP})_2$, we next examined
 105 its electrical conductivity as this is a further key requirement for EDLC electrodes. The electrical
 106 conductivity of a pressed pellet of $\text{Cu}_3(\text{HHTP})_2$ (two-point probe) was measured as 0.007 S cm^{-1}
 107 (see SI Methods). This is comparable to previously reported values for this MOF ($0.0001 - 0.3$
 108 S cm^{-1} for polycrystalline samples).^{21,28,31,36} Composite films of $\text{Cu}_3(\text{HHTP})_2$ (85 wt. % $\text{Cu}_3(\text{HHTP})_2$,
 109 10 wt. % carbon black, and 5 wt. % PTFE) of ca. 250 μm thickness were then prepared by
 110 adapting the traditional literature method for the preparation of activated carbon (AC) films (see
 111 SI Methods).³⁷ Carbon black was used as a conductive additive to increase the electrical
 112 conductivity of the film for use in EDLCs and has negligible contribution to the total capacitance
 113 of the cell (SI Fig. S5). Films made without the conductive additive (95 wt. % $\text{Cu}_3(\text{HHTP})_2$ and 5

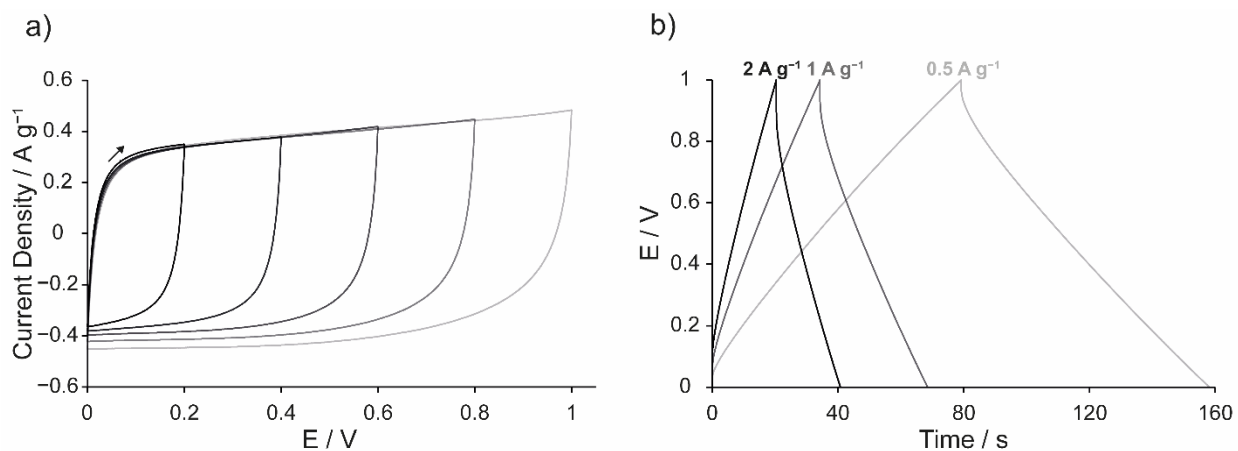


Fig. 2 (a) Cyclic voltammograms (CVs) at a scan rate of 10 mV s^{-1} up to 1.0 V show that $\text{Cu}_3(\text{HHTP})_2$ displays predominantly double-layer capacitive behaviour in this voltage window in symmetric EDLCs with $1 \text{ M NEt}_4\text{BF}_4$ in acetonitrile electrolyte. The black arrow shows the direction of scanning from the start of the scan. (b) Galvanostatic charge-discharge (GCD) profiles at a variety of current densities confirm this behaviour (see labels).

114 wt. % PTFE) displayed highly resistive behaviour in EDLCs and required very low current
 115 densities for analysis, showing the necessity of the conductive additive to achieve good capacitive
 116 performance (SI Figs. S6, S7). This indicates a limitation of using this MOF in EDLCs.
 117 Interestingly, Cu K-edge XANES on pristine film samples revealed evidence for the presence of
 118 Cu(I), with the amount of Cu(I) observed varying between samples (SI Fig. S8). Linear
 119 combination fitting of this XANES data with standard compounds indicated a maximal Cu(I)
 120 content of approximately 20 % (SI Fig. S9; Table S2). This underscores the sensitivity of
 121 $\text{Cu}_3(\text{HHTP})_2$ and modification of the film-making procedure could be considered in future work if
 122 Cu(I) content proves to be problematic.

123 To investigate the electrochemical double-layer capacitance of $\text{Cu}_3(\text{HHTP})_2$, symmetrical
 124 EDLCs were assembled using composite $\text{Cu}_3(\text{HHTP})_2$ film electrodes and $1 \text{ M NEt}_4\text{BF}_4$ in
 125 acetonitrile electrolyte (see SI Methods). Cyclic voltammograms (CVs) and galvanostatic charge-
 126 discharge (GCD) experiments on these cells showed nearly rectangular and triangular traces
 127 respectively (**Fig. 2**), indicative of electrochemical double-layer capacitance. An initial cell voltage
 128 window of approximately 1.0 V , where primarily electric double-layer behaviour was observed,
 129 was established for $\text{Cu}_3(\text{HHTP})_2$ by running CVs with progressively higher final voltages. Beyond
 130 1.0 V , faradaic processes centred at ca. 1.1 V were observed (SI Fig. S10). This stable voltage
 131 window was confirmed by running CVs of $\text{Cu}_3(\text{HHTP})_2$ composite electrodes in a three-electrode
 132 arrangement with $1 \text{ M NEt}_4\text{BF}_4$ in acetonitrile. Electric double-layer capacitive behaviour and no
 133 faradaic activity were observed for $\text{Cu}_3(\text{HHTP})_2$ between the open circuit potential of $+0.33 \text{ V}$ and
 134 -0.27 V vs. Ag in the anodic direction, and between the open circuit potential of $+0.19 \text{ V}$ and

135 +0.79 V vs. Ag in the cathodic direction (SI Figs. S11, S12). This is consistent with a working
136 voltage window for $\text{Cu}_3(\text{HHTP})_2$ EDLCs of approx. 1.0 – 1.2 V, which is further discussed below.
137 This sharply contrasts to traditional activated carbons, which have a larger typical working voltage
138 window of ca. 2.5 V with this electrolyte.³⁸

139 To evaluate and compare the capacitive performance of $\text{Cu}_3(\text{HHTP})_2$ with other electrode
140 materials, specific capacitance (C_g) was calculated at a variety of current densities from GCD
141 profiles using the *Supycap* Python code (see SI Methods). At a low current density of 0.04 – 0.05
142 A g^{-1} , the specific capacitance of $\text{Cu}_3(\text{HHTP})_2$ in EDLCs as assembled above was recorded as
143 110 – 114 F g^{-1} when charged between 0 – 1 V (SI Fig. S13, Table S3). This value is very similar
144 to that recorded previously for the almost isostructural framework $\text{Ni}_3(\text{HITP})_2$ at a similar current
145 density (111 – 116 F g^{-1}) in a similar EDLC with 1 M NEt_4BF_4 in acetonitrile.²⁷ Increasing the
146 current density leads to a decrease in the specific capacitance (**Fig. 3**), again with very similar
147 results to those reported for $\text{Ni}_3(\text{HITP})_2$. Interestingly, these results suggest that the identity of the
148 metal node (Cu or Ni) and ligating heteroatom (O or N) have little/no impact on the double-layer
149 capacitance of these two frameworks. Indeed, $\text{Ni}_3(\text{HITP})_2$ and $\text{Cu}_3(\text{HHTP})_2$ have very similar 3D
150 structures, with both formed from the eclipsed or near-eclipsed stacking of 2D π -d conjugated
151 layers.^{18,31,39} Therefore, our results suggest high capacitive performance arises from the three-
152 dimensional structures of these MOFs. These results further suggest that the capacitance of an
153 EDLC is uniquely defined by the 3D structure of the electrode and the electrolyte used. This
154 generality has not been previously demonstrated using porous carbon materials, although further
155 work is needed to confirm this hypothesis. The equivalent series resistances (*ESRs*) of the EDLC
156 cells were measured using both electrochemical impedance spectroscopy (EIS) and GCD
157 profiles, with *ESRs* of between 7 – 18 Ω obtained for a range of cells (SI Fig. S14).

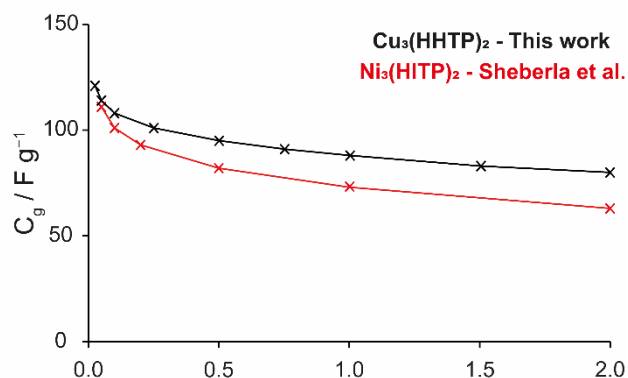


Fig. 3 Comparison of specific capacitance versus current density graphs for $\text{Cu}_3(\text{HHTP})_2$ and $\text{Ni}_3(\text{HITP})_2$ (literature)²⁷. This demonstrates the similarity in the capacitance of these MOFs in similar symmetric EDLCs.

158 Furthermore, we note higher capacitance retention (79 % between 0.25 – 2 A g⁻¹; 72 %
159 between 0.25 – 2.5 A g⁻¹) than obtained in previous studies using Cu₃(HHTP)₂ powder electrodes
160 in symmetric solid-state EDLCs (30 % up to 2 A g⁻¹), and capacitance retention on par with that
161 obtained with Cu₃(HHTP)₂ NWAs in aqueous (58 % up to 2.5 A g⁻¹) and solid-state (60 % up to 2
162 A g⁻¹) EDLCs.^{28,29} Although a direct comparison with solid-state cells is difficult due to the different
163 phases of the electrolytes, these results illustrate that high capacitive behaviour can be achieved
164 using Cu₃(HHTP)₂ powder and a conductive additive, which has a simpler synthesis than NWAs
165 (SI Fig. S15). However, it must be noted that higher specific capacitances were observed for
166 devices constructed with NWA electrodes (120 F g⁻¹ at 0.5 A g⁻¹ with a solid-state electrolyte; 195
167 F g⁻¹ at 0.5 A g⁻¹ with aqueous electrolyte) than observed in this work.^{28,29}

168 Another common metric used to compare EDLC performance of electrode materials is the
169 areal (surface area normalized) capacitance. In this work, the areal capacitance of Cu₃(HHTP)₂
170 was calculated as approx. 14 μF cm⁻² at 0.05 A g⁻¹. Although this is lower than that reported for
171 Ni₃(HITP)₂ (18 μF cm⁻²), significant variation in our values between 14 and 23 μF cm⁻² was
172 observed for EDLCs prepared using independent samples of Cu₃(HHTP)₂ with different BET
173 surface areas (SI Table S4). We also observed variations in the performances of assembled
174 EDLCs as a function of the areal mass loading of the electrodes. In general, EDLCs with higher
175 areal mass loadings exhibited a more rapid decrease in capacitance as a function of current
176 density and a higher ESR than those with lower areal mass loadings (SI Fig. S13, Table S3). This
177 is consistent with previous observations but highlights the need for clear communication on mass
178 loadings when comparing electrode performances.⁴⁰

179 To further investigate the suitability of Cu₃(HHTP)₂ for both practical supercapacitor
180 applications and structure-property investigations, the voltage limits and cycling stability were
181 studied in more detail. To probe the voltage limits of the cell, GCD experiments at a current density
182 of 0.1 A g⁻¹ were run with increasing final cell voltages from 0.6 V until the failure of the cell was
183 observed. This showed an initial consistent increase in the specific capacitance with increasing
184 final voltage followed by a rapid decrease upon cycling beyond 1.3 V (**Fig. 4a**). This demonstrates
185 that the voltage limit of Cu₃(HHTP)₂ in a symmetric EDLC is approximately 1.3 V under these
186 charging/discharging conditions, beyond which rapid degradation of the Cu₃(HHTP)₂ electrodes
187 occurs causing irreversible loss in capacitance. Rapid capacitance loss when cycling above this
188 cell voltage was confirmed via CV experiments cycling up to cell voltages of 1.6 V (SI Fig. S16).
189 Degradation was confirmed by examining the Cu K-edge XANES of Cu₃(HHTP)₂ composite
190 electrodes from an EDLC held at a cell voltage of 1.5 V for 1 h (SI Fig. S17). A shift of the

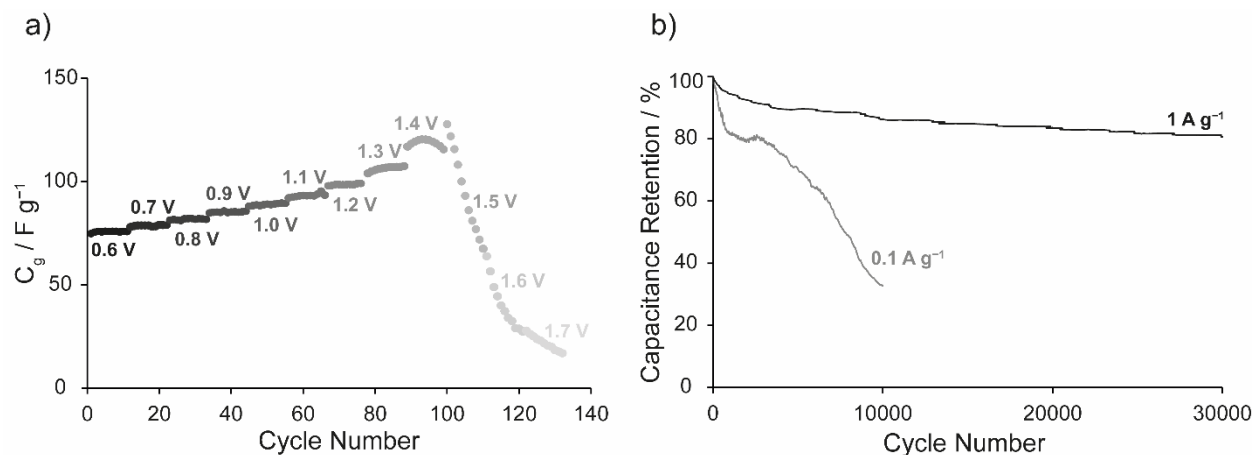


Fig. 4 (a) Specific capacitance, calculated from GCD profiles, against cycle number for increasing final cell voltages (see labels). This illustrates the voltage limit of the symmetric $\text{Cu}_3(\text{HHTP})_2$ EDLC. (b) Capacitance retention as a function of cycle number when cycling at 1 A g^{-1} and 0.1 A g^{-1} up to 1.0 V.

191 absorption edge to a lower energy, in addition to the appearance of an inflection at ca. 8981 eV,
 192 indicate formation of Cu(I) in the negative electrode. In the positive electrode, the appearance of
 193 the feature at ca. 8981 eV indicates a significant change in the coordination environment around
 194 Cu to a lower symmetry environment. The shift of the rising edge to higher energies suggests an
 195 oxidation process may occur in the positive electrode too. These results indicate fundamental
 196 changes to the MOF structure in both electrodes and hint at potential degradation mechanisms,
 197 although further work is required to study these processes in more detail.

198 To further explore the working voltage window of $\text{Cu}_3(\text{HHTP})_2$ EDLCs, Cu K-edge XANES
 199 studies were carried out on electrodes extracted from EDLCs held at different cell voltages for a
 200 period of 1 h (SI Fig. S18). For a cell voltage of 0.5 V, minimal changes were observed in
 201 the XANES spectra. However, for a cell voltage of 0.8 V, the XANES data suggest structural
 202 changes to $\text{Cu}_3(\text{HHTP})_2$ in the positive electrode. This suggests that kinetically slow faradaic
 203 processes may occur at cell voltages below 1.1 V but are missed due to the scan rates used in
 204 the above electrochemistry experiments (**Fig. 2**). This hypothesis was confirmed by obtaining a
 205 CV at a scan rate of 0.1 mV s^{-1} up to 1 V, with faradaic activity observed at this slow scan rate
 206 upon cycling past 0.8 V (SI Fig. S19). This highlights that $\text{Cu}_3(\text{HHTP})_2$ may only be kinetically
 207 stable up to 1 V, a possible limitation that is explored further below.

208 Finally, the cycling stability of symmetric $\text{Cu}_3(\text{HHTP})_2$ EDLCs was investigated at two different
 209 current densities in GCD experiments limited to a maximum cell voltage of 1 V. Reasonable
 210 cycling stability was observed when cycled between 0 – 1 V at 1 A g^{-1} , with capacitance retention
 211 of 81 % over 30,000 cycles (**Fig. 4b**). The capacitance retentions after 5,000 and 10,000 cycles

212 (90 % and 86 %, respectively) compare well with those of $\text{Ni}_3(\text{HITP})_2$, approx. 90% over 10,000
213 cycles, and $\text{Cu}_3(\text{HHTP})_2$ NWA devices with an aqueous electrolyte, 79.9 % over 5,000 cycles (SI
214 Figs. S20, S21).^{27,29} This further highlights the similarities in electrochemical performance
215 between $\text{Ni}_3(\text{HITP})_2$ and $\text{Cu}_3(\text{HHTP})_2$, and is further evidence that electrodes manufactured from
216 $\text{Cu}_3(\text{HHTP})_2$ powder can achieve high EDLC performance on par with those made with
217 $\text{Cu}_3(\text{HHTP})_2$ NWAs. Cu K-edge XANES showed minimal changes to the edge position and pre-
218 edge peaks following this cycling, confirming the stability of $\text{Cu}_3(\text{HHTP})_2$ upon extensive cycling
219 at this current density (SI Fig. S22).

220 However, the capacitance retention of $\text{Cu}_3(\text{HHTP})_2$ is significantly lower than that of YP50F, a
221 commercial microporous AC, when cycled in an EDLC with 1 M NEt_4BF_4 in acetonitrile. In our
222 work, YP50F exhibited a capacitance retention of 99 % over 10,000 cycles when cycled between
223 0 – 2.5 V at 2 A g^{-1} (SI Figs. S23, S24). This illustrates that, while this family of MOFs have specific
224 and areal capacitances on par or exceeding current state-of-the-art carbons (YP50F displays a
225 specific capacitance of ca. 90 – 100 F g^{-1} in this system), significant improvement is required to
226 achieve comparable cycling stability. This is the first work to call attention to this key difference
227 and illustrates a major disadvantage of using this family of conductive MOFs in EDLCs instead of
228 ACs, as high cycling stability is a crucial property of an EDLC. Furthermore, the capacitance
229 retention of $\text{Cu}_3(\text{HHTP})_2$ EDLCs in this work was significantly lower when cycled at a lower current
230 density of 0.1 A g^{-1} , with only 32 % capacitance retention after 10,000 cycles (**Fig. 4b**). Cu K-
231 edge XANES of the positive electrode following this cycling again provided evidence for a change
232 in the MOF structure, confirming degradation at this current density and further emphasizing that
233 $\text{Cu}_3(\text{HHTP})_2$ is only kinetically stable when cycled between 0 – 1 V (SI Fig. S25). This is also the
234 first work to highlight the difference in capacitance retention at different current densities with this
235 family of conducting frameworks. These findings raise questions about the practical applicability
236 of these frameworks in commercial devices. Future studies to identify the degradation
237 mechanisms in these frameworks may allow for the design of conductive MOFs with wider double-
238 layer stability windows, and thus improved capacitive performances. Given the observation of
239 redox processes centred on the Cu nodes by XANES, varying the metal node or organic linker
240 molecule may be a viable method to increase the potential window.⁴¹

241 **Conclusion**

242 We have demonstrated that the conductive MOF $\text{Cu}_3(\text{HHTP})_2$ displays good capacitive behaviour
243 in symmetric EDLCs with 1 M NEt_4BF_4 in acetonitrile, with a specific capacitance of 110 – 114
244 F g^{-1} at 0.04 – 0.05 A g^{-1} recorded. Our work shows that the previously observed capacitive
245 behaviour of $\text{Ni}_3(\text{HITP})_2$ is not unique amongst layered conducting MOFs and has expanded the
246 family of conductive MOFs which is known to display capacitive performance in EDLCs with
247 organic electrolytes. Notably, $\text{Cu}_3(\text{HHTP})_2$ can be synthesized using all commercially available
248 starting materials, and we have demonstrated that standard electrode fabrication techniques
249 using $\text{Cu}_3(\text{HHTP})_2$ powder can be employed with this framework to achieve good capacitive
250 performance, making this framework an accessible model system for further study. The similarity
251 in the specific capacitances of $\text{Cu}_3(\text{HHTP})_2$ and $\text{Ni}_3(\text{HITP})_2$ at low current densities with the same
252 organic electrolyte shows that the capacitive performance is independent of the identity of the
253 metal node and organic linker molecule for these two nearly isostructural frameworks. Importantly,
254 this suggests that the capacitive performance of an EDLC more generally is uniquely defined by
255 the 3D structure of the electrodes and the electrolyte, although further work is required to test this
256 significant hypothesis. Finally, our work also illustrates several limitations of using current
257 conductive MOFs in EDLCs, notably the significantly lower cycling stability and stable double-
258 layer voltage window relative to state-of-the-art carbon materials. This raises questions about the
259 practical applicability of these frameworks in commercial devices. Ultimately our work will guide
260 the design of next generation metal-organic frameworks with improved energy storage
261 performance.

262 **Experimental Section**

263 **Materials**

264 Starting materials were purchased from Sigma-Aldrich and used without modification unless stated. Ethanol
265 was purchased from VWR International. Aqueous ammonia (35 %) solution and acetone were purchased
266 from Fischer Scientific. YP50F was purchased from Kuraray. Acetylene black carbon ($\text{SA} = 75 \text{ m}^2 \text{ g}^{-1}$) was
267 purchased from Alfa Aesar. 2,3,6,7,10,11-hexahydroxytriphenylene hydrate ($\text{H}_6\text{HHTP} \cdot x\text{H}_2\text{O}$) was
268 purchased from TCI. Tetraethylammonium tetrafluoroborate (NEt_4BF_4) was dried under vacuum at 100 °C
269 for 48 h before transferring to a N_2 -filled glovebox. Anhydrous acetonitrile was purged with N_2 for 3 h before
270 taking it into a N_2 -filled glovebox, where it was further dried by the addition of activated 3 Å molecular sieves.
271 Sieves were activated at 250 °C in a vacuum oven for 12 h prior to transferring into a N_2 -filled glovebox.

272

273

274 **Synthesis of Cu₃(HHTP)₂**

275 Cu₃(HHTP)₂ was synthesized by modifying a recently published literature procedure.³⁰ A solution of
276 Cu(NO₃)₂·3H₂O (0.127 g, 0.526 mmol, 1.65 eq) and aqueous ammonia (35 %) solution (0.829 mL, 15.0
277 mmol, 47 eq) in distilled water (2 mL) was prepared. The resulting dark blue solution was added dropwise
278 to a dispersion of 2,3,6,7,10,11-hexahydroxytriphenylene hydrate, H₆HHTP·xH₂O, (0.103 g, 0.318 mmol,
279 1.00 eq) in distilled water (8.4 mL). The resulting mixture was heated in a furnace oven in a 40 mL screw
280 vial (Thermo Scientific; B7999-6), closed with a screw cap fitted with a septum as a safety precaution in the
281 event of over pressurization, at 80 °C for 24 h. The dark blue precipitate formed was separated by
282 centrifugation, and the supernatant layer was discarded. The dark blue precipitate was then washed
283 successively with water (3 × 30 mL), ethanol (4 × 30 mL), and acetone (4 × 30 mL). Washing was performed
284 by centrifuging the precipitate with the desired washing solvent for 15 – 30 minutes before removing the
285 supernatant layer and replacing with fresh washing solvent. No soaking of the precipitate was performed.
286 The resulting dark blue powder was dried at 75 °C under dynamic vacuum for 72 h and then stored in a N₂-
287 filled glovebox until used.

288 We found that rapid washing (completed in ca. 5 h) and activation of the synthesized Cu₃(HHTP)₂ to
289 minimize its exposure to air was required to ensure a high porosity and a wider stable double-layer voltage
290 window.

291

292 **Elemental Analysis**

293 Laboratory elemental analysis was performed on Cu₃(HHTP)₂ as synthesized above by the Microanalysis
294 Facility at the Yusuf Hamied Department of Chemistry, Cambridge .

295 Cu content was determined via inductively coupled plasma optical emission spectroscopy (ICP-OES) using
296 a Thermo Scientific iCAP-7400 ICP spectrometer. 1.3610 mg of Cu₃(HHTP)₂ was digested in 5 mL of
297 concentrated HNO₃ (67 – 69 %, trace metal, Fisher Scientific), and the sample diluted with 5 mL of water.
298 A 0.5 mL aliquot was then diluted to 10 mL with water. Cu concentration of the resulting solution was
299 determined using calibration curves constructed from standard solutions (Multi-element standard solution
300 for ICP IV, Fisher Scientific). C, H and N content was determined via CHN combustion analysis using an
301 Exeter Analytical CE-440, with combustion at 975 °C.

302 Calculated for Cu₃(HHTP)₂: Cu, 23.1 wt. %; C, 52.3 wt. %; H, 1.5 wt. %.

303 Experimental results for Cu₃(HHTP)₂ synthesized above: Cu, 21.7 wt. %; C, 48.9 wt. %; H, 2.4 wt. %; N,
304 2.8 wt. %.

305 These results confirm that the as-synthesized Cu₃(HHTP)₂ has approximately the correct stoichiometric
306 ratio of Cu and HHTP. It also indicates the potential presence of a N-containing impurity leftover in the MOF
307 following washing.

308 **X-ray Diffraction**

309 Laboratory powder X-ray diffraction data were collected on a Malvern Panalytical Empyrean instrument,
310 equipped with an X'celerator Scientific detector using non-monochromated Cu K α radiation ($\lambda = 1.5418 \text{ \AA}$).
311 Borosilicate glass capillary tubes (0.5 mm outside diameter, 0.01 mm wall thickness; Capillary Tube
312 Supplies Ltd.) were loaded with the sample in a N $_2$ -filled glovebox, with NiCr wire used to aid packing. The
313 capillary was then sealed in the N $_2$ -filled glovebox using EA 3430 epoxy adhesive (Loctite), which was
314 allowed to cure for 5 h before removing the capillary from the glovebox. The data were collected at room
315 temperature over a 2θ range of 3 – 50 $^\circ$, with an effective step size of 0.017 $^\circ$ and a total collection time per scan
316 of 1 h. Multiple scans were chosen to minimize the possibility of saturating the detector as well as to detect
317 any possible changes with time (none were observed). The presented experimental PXRD is a sum
318 average of 15 scans.

319 Simulated PXRD patterns were produced using GSAS-II Crystallography Data Analysis Software.⁴²
320 Computational structures used to produce the simulated PXRD patterns and XANES are available at:
321 <https://doi.org/10.5281/zenodo.4694845>

322

323 **Gas Adsorption Measurements**

324 Low pressure N $_2$ isotherms (adsorption and desorption) were collected using a Micromeritics 3Flex at 77
325 K. Prior to analysis, samples were degassed in a Schlenk flask at 80 $^\circ\text{C}$ for 24 h. In-situ degassing (80 $^\circ\text{C}$,
326 24 h) was further performed on a Micromeritics VacPrep. Material BET areas were calculated from the
327 isotherms using the BET equation and Rouquerol's consistency criteria implemented in BETSI.^{32, 43} The
328 micropore volume (W_0) and the total (V_{tot}) pore volumes were calculated at P/P_0 of 0.1 and 0.99,
329 respectively. For Cu $_3$ (HHTP) $_2$, a Type I N $_2$ isotherm was observed, with high gas uptake below 0.1 P/P_0
330 indicating extensive microporosity. See the Appendix for full BETSI readouts.

331

332 **Conductivity Measurements**

333 The electrical conductivity of Cu $_3$ (HHTP) $_2$ samples was measured via a two-point probe method using a
334 homemade set-up. Samples were pressed between two stainless steel electrodes using a hydraulic press
335 (Specac). Insulating PTFE disks were used to prevent a short circuit through the press. All measurements
336 were conducted with a loading of between 1.50 – 1.57 ton-force cm $^{-2}$. Resistances were measured using
337 a Keithley 2000 Multimeter.

338 The conductivity, σ (S cm $^{-1}$), of the sample was calculated according to: $\sigma = L / RA$, where L is the thickness
339 of the sample (cm), A is the area of the sample (cm 2), and R is the measured resistance (Ω). All values of
340 L and A were measured following completion of the measurement, assuming a non-elastic material. Based

341 on multiple measurements of the resistance and the thickness of the sample, the error on the calculated
342 conductivity value is ca. $\pm 6.6\%$.

343 Pellets composed of $\text{Cu}_3(\text{HHTP})_2$ were prepared by loading the material into a 13 mm Evacuatable Pellet Die
344 (Specac) and applying a force of 3 ton-force cm^{-2} for 5 mins with a hydraulic press (Specac). The areal
345 mass loading of the pellets was approximately 50 mg cm^{-2} . The thickness of the pellets was measured
346 using a digital micrometer (Mitutoyo) as approximately $330 \mu\text{m}$.

347 **Electrode Film Preparation**

348 Freestanding composite MOF films were prepared by adapting the traditional literature method for activated
349 carbons.¹¹ $\text{Cu}_3(\text{HHTP})_2$ powder and acetylene black were lightly ground together in a vial before ethanol
350 (ca. 1.5 mL) was added to produce a loose slurry. This was sonicated for 15 mins before being added to
351 PTFE dispersion (60 wt. % in water) in a few drops of ethanol in a watchglass. The slurry was stirred by
352 hand in the watchglass for 40 mins in ambient conditions. The film was gradually formed upon drying of the
353 slurry before being transferred to a glass surface, where it was kneaded for 20 mins to ensure homogenous
354 incorporation of the active materials and PTFE and then rolled into a freestanding film using a homemade
355 aluminium rolling pin. The film was dried in vacuo at 75°C for at least 48 h to remove any remaining ethanol.
356 The masses of components were calculated so that the final film had a composition of 85 wt. % $\text{Cu}_3(\text{HHTP})_2$,
357 10 wt. % acetylene black, and 5 wt. % PTFE.

358 Freestanding acetylene black, YP50F, and $\text{Cu}_3(\text{HHTP})_2$ films were prepared using the same technique.
359 These had a final composition of 95 wt. % electroactive material and 5 wt. % PTFE.

360

361 **EDLC Assembly**

362 Symmetric electric double-layer capacitors (EDLCs) with $\text{Cu}_3(\text{HHTP})_2$ composite and acetylene black film
363 electrodes were prepared in Swagelok PFA-820-6 union tube fittings with homemade stainless-steel plugs
364 as current collectors. Electrodes were cut from freestanding films in a N_2 -filled glovebox using a $\frac{1}{4}$ " stainless
365 steel manual punching cutter (Hilka Tools), with areal mass loadings ranging between $10 - 35 \text{ mg cm}^{-2}$. An
366 excess of 1 M tetraethylammonium tetrafluoroborate (NEt_4BF_4) in anhydrous acetonitrile was used as an
367 electrolyte. This solution was prepared in a N_2 -filled glovebox. Whatman glass microfiber filter (GF/A), cut
368 with a $\frac{3}{8}$ " stainless steel manual punching cutter, was used as separator. This was dried in vacuo at 100
369 $^\circ\text{C}$ for 24 h prior to use. EDLCs were hand-sealed until air-tight before being removed from the glovebox
370 for electrochemical testing.

371 Symmetric electric double-layer capacitors (EDLCs) with YP50F film electrodes were prepared as coin cells
372 in CR2032 SS316 coin cell cases (Cambridge Energy Solutions). Electrodes were cut from freestanding
373 YP50F films with areal mass loadings ranging between $10 - 15 \text{ mg cm}^{-2}$. The electrodes were dried in
374 vacuo at 100°C for at least 24 h prior to assembling the cell in a N_2 -filled glovebox. A 1 M solution of

375 NEt_4BF_4 in anhydrous acetonitrile was used as an electrolyte. This solution was prepared in a N_2 -filled
376 glovebox. Whatman glass microfiber filter (GF/A) was used as separator. This was dried in vacuo at 100
377 $^\circ\text{C}$ for 24 h prior to use. Each coin cell contained two SS316 separator disks and one SS316 spring to
378 ensure sufficient pressure in the cell. The coin cells were sealed in the glovebox using a Compact Hydraulic
379 Coin Cell Crimper (Cambridge Energy Solutions).

380 $\text{Cu}_3(\text{HHTP})_2$ composite cells were assembled in Swagelok PFA-820-6 union tube fittings as opposed to in
381 CR2032 SS316 coin cell cases (Cambridge Energy Solutions) as the disassembly of the cell, without
382 inadvertently causing cell discharge, was easier with the tube fittings.

383

384 **Three-Electrode Cell Assembly**

385 Three-electrode cells were prepared in Swagelok PFA-820-3 union tube fittings with homemade stainless-
386 steel plugs as current collectors. $\text{Cu}_3(\text{HHTP})_2$ composite electrodes with areal mass loadings ranging
387 between 12 – 20 mg cm^{-2} were used as working electrodes. Overcapacitive YP50F activated carbon film
388 electrodes with areal mass loadings of 35 – 40 mg cm^{-2} were used as counter electrodes. Ag wire was
389 used as a pseudo-reference electrode. A 1 M solution of tetraethylammonium tetrafluoroborate (NEt_4BF_4)
390 in anhydrous acetonitrile was used as an electrolyte. All measurements were performed under dry and
391 oxygen-free conditions in a N_2 -filled glove box. Under these conditions, the ferrocene–ferricenium (Fc/Fc^+)
392 redox couple was measured at 0.63 ± 0.01 V versus Ag. All potentials discussed for the three-electrode cell
393 are referenced to Ag.

394

395 **Electrochemical Characterization**

396 All electrochemical measurements were carried out using Biologic SP-150 and VSP-3e potentiostats and
397 a Biologic BCS-800 Series ultra-precision battery cycler. Electrochemical Impedance Spectroscopy (EIS)
398 measurements were performed in the frequency range from 200 kHz to 3 – 10 mHz using a single-
399 sinusoidal signal with a sinus amplitude of 10 mV. No drift correction was applied. The specific capacitance,
400 C_g (F g^{-1}), was calculated from galvanostatic charge-discharge (GCD) discharge profiles using the *Supycap*
401 Python code. C_g values were determined using only the mass of active material (i.e., Cu_3HHTP_2) in the
402 EDLCs.

403 The equivalent series resistance (*ESR*) was calculated from both Nyquist plots (produced from EIS
404 measurements) and from the voltage drop at the beginning of GCD discharge profiles. For the calculation
405 from Nyquist plots, the *ESR* was obtained from extrapolation of the low frequency response onto the real
406 ($\text{Re}(Z)$) axis, as is consistent with the literature.⁴⁴ For the calculation from GCD discharge profiles, the
407 *Supycap* Python code was used.

408 Current densities were calculated by dividing the current applied during the GCD experiment, I , by the
409 average mass of active material per electrode, \bar{m} .

410 For full details of the calculations and methods used in the *Supycap* Python code, please visit: [GitHub -](#)
411 [AdaYuanChen/Supycap: Analysis tool for the CC and CV experiment of supercapacitors](#)

412

413 **X-ray Absorption Spectroscopy**

414 Cu K-edge X-ray absorption near edge structure (XANES) measurements were performed at the B18
415 beamline at Diamond Light Source. Measurements at the Cu K-edge were recorded in fluorescence yield
416 mode. Energy calibration was done with Cu metal as a reference. XANES data were processed and
417 analysed using the Athena program of the Demeter software package.⁴⁵

418 XANES electrode samples were prepared from the disassembly of EDLC cells. The cells were
419 disassembled in a N₂-filled glovebox and the electrodes were isolated and packaged into air-tight foil/poly
420 pouches (Sigma-Aldrich). Cu(I) standard samples (Cu₂O, CuOAc) were prepared by grinding a small
421 amount (ca. 5 wt. %) of the standard with cellulose in a N₂-filled glovebox before packaging into an air-tight
422 foil/poly pouch. Cu(II) standard samples (CuO, Cu(OAc)₂) were prepared by grinding a small amount of the
423 standard (ca. 5 wt. %) with cellulose in ambient conditions before pressing into a pellet using a hydraulic
424 press (Specac) as described previously.

425 In this work, the edge is defined as the energy at normalized $x\mu(E) = 0.5$.

426 XANES calculations were done using the FEFF 9.0 code.^{46, 47} The Full Multiple Scattering (*FMS*) and Self
427 Consistent Field (*SCF*) radii were set to 8.0 Å and 7.5 Å respectively and calculations were done using the
428 Hedin-Lundqvist exchange correlation potential. The exchange potential was offset by 2 eV to account for
429 errors in the calculated Fermi level, and an imaginary energy of 0.5 eV was added to correct for instrumental
430 broadening. All other FEFF parameters were set to the default values. A red shift of the simulated spectra
431 was required to align it with the experimental spectrum.

432 **Author Contributions**

433 J.W.G. and A.C.F. designed the research. J.W.G and C.J.B. performed the material synthesis
434 and electrode film fabrication. M.J.G. performed the crystal structure modelling. J.W.G, C.J.B.
435 and M.J.G performed and interpreted the PXRD measurements. D.G.M. performed and
436 interpreted the N₂ gas adsorption measurements. J.W.G and C.L. performed the conductivity
437 measurements. J.W.G performed the electrochemical cell assemblies. J.W.G and Y.C.
438 interpreted the electrochemical cell characterisation measurements. S.B. and J.W.G interpreted
439 the XANES measurements. S.B. performed and interpreted the XANES modelling. All authors
440 interpreted the results and contributed to the writing of the manuscript.

441 **Conflicts of interest**

442 There are no conflicts to declare.

443 **Acknowledgements**

444 J.W.G. acknowledges the School of the Physical Sciences (Cambridge) for the award of an
445 Oppenheimer Studentship. This work was supported by the Faraday Institution [grant number
446 FIRG017], via a Faraday Undergraduate Summer Experience (FUSE) internship to Y.C. The work
447 at Imperial (A.W.) was supported by a Royal Society University Research Fellowship (UF100278)
448 and benefited from the UK Materials and Molecular Modelling Hub for computational resources,
449 which is partially funded by EPSRC (EP/P020194/1 and EP/T022213/1). M.J.G. thanks the Royal
450 Society for PhD funding. D.F.-J. thanks the European Research Council (ERC) under the
451 European Union's Horizon 2020 Research and Innovation Programme (NanoMOFdeli), ERC-
452 2016-COG 726380, and Innovate UK (104384). S.E.D. acknowledges funding from the Winton
453 Programme for the Physics of Sustainability (Cambridge). A.C.F. thanks the Isaac Newton Trust
454 of Trinity College (Cambridge) for a Research Grant (G101121), and the Yusuf Hamied
455 Department of Chemistry (Cambridge) for the award of a BP Next Generation Fellowship. This
456 work was also supported by a UKRI Future Leaders Fellowship to A.C.F. (MR/T043024/1). We
457 thank the Diamond Light Source for the award of beam time as part of the Energy Materials Block
458 Allocation Group SP14239. We thank Dr. Phillip Milner and Dr. Lewis Owen for collaboration and
459 stimulating discussion over the course of the project. We thank Dr. Chris Truscott and Dr. Nigel
460 Howard for collaboration and technical expertise.

461 **References**

- 462 1. IEA, *World Energy Outlook 2019*, 2019, OECD Publishing,
463 <https://doi.org/10.1787/caf32f3b-en>.
- 464 2. A. Z. al Shaqsi, K. Sopian and A. Al-Hinai, *Energy Rep.*, 2020, **6**, 288–306.
- 465 3. T. M. Gü, *Energy Environ. Sci.*, 2018, **11**, 2696.
- 466 4. A. González, E. Goikolea, J. A. Barrena and R. Mysyk, *Renew. Sustain. Energy Rev.*,
467 2016, **58**, 1189–1206.
- 468 5. P. Simon, Y. Gogotsi and B. Dunn, *Science*, 2014, **343**, 1210–1211.
- 469 6. X. Liu and K. Li, *Transportation Safety and Environment*, 2020, **2**, 183–201.
- 470 7. E. E. Miller, Y. Hua and F. H. Tezel, *J. Energy Storage*, 2018, **20**, 30–40.
- 471 8. T. Méndez-Morales, N. Ganfoud, Z. Li, M. Haefele, B. Rotenberg and M. Salanne, *Energy*
472 *Stor. Mater.*, 2019, **17**, 88–92.
- 473 9. J. Chmiola, G. Yushin, R. Dash and Y. Gogotsi, *J. Power Sources*, 2006, **158**, 765–772.

- 474 10. C. Largeot, C. Portet, J. Chmiola, P. L. Taberna, Y. Gogotsi and P. Simon, *J. Am. Chem.*
475 *Soc.*, 2008, **130**, 2730–2731.
- 476 11. J. Chmiola, G. Yushin, Y. Gogotsi, C. Portet, P. Simon and P. L. Taberna, *Science*, 2006,
477 **313**, 1760–1763.
- 478 12. T. A. Centeno, O. Sereda and F. Stoeckli, *Phys. Chem. Chem. Phys.*, 2011, **13**, 12403–
479 12406.
- 480 13. F. Stoeckli and T. A. Centeno, *J. Mater. Chem. A*, 2013, **1**, 6865–6873.
- 481 14. E. Raymundo-Piñero, K. Kierzek, J. Machnikowski and F. Béguin, *Carbon*, 2006, **44**,
482 2498–2507.
- 483 15. J. Liu, X. Song, T. Zhang, S. Liu, H. Wen and L. Chen, *Angew. Chem. Int. Ed.*, 2020, **60**,
484 5612–5624.
- 485 16. L. S. Xie, G. Skorupskii and M. Dincă, *Chem. Rev.*, 2020, **120**, 8536–8580.
- 486 17. M. Hmadeh, Z. Lu, Z. Liu, F. Gándara, H. Furukawa, S. Wan, V. Augustyn, R. Chang, L.
487 Liao, F. Zhou, E. Perre, V. Ozolins, K. Suenaga, X. Duan, B. Dunn, Y. Yamamoto, O.
488 Terasaki and O. M. Yaghi, *Chem. Mater.*, 2012, **24**, 3511–3513.
- 489 18. M. Ko, L. Mendecki and K. A. Mirica, *Chem. Commun.*, 2018, **54**, 7873–7891.
- 490 19. L. Sun, M. G. Campbell and M. Dincă, *Angew. Chem. Int. Ed.*, 2016, **55**, 3566–3579.
- 491 20. J.-H. Dou, M. Q. Arguilla, Y. Luo, J. Li, W. Zhang, L. Sun, J. L. Mancuso, L. Yang, T. Chen,
492 L. R. Parent, G. Skorupskii, N. J. Libretto, C. Sun, M. C. Yang, P. V. Dip, E. J. Brignole, J.
493 T. Miller, J. Kong, C. H. Hendon, J. Sun and M. Dincă, *Nat. Mater.*, 2021, **20**, 222–228.
- 494 21. K. W. Nam, S. S. Park, R. dos Reis, V. P. Dravid, H. Kim, C. A. Mirkin and J. F. Stoddart,
495 *Nat. Commun.*, 2019, **10**, 4948.
- 496 22. D. Feng, T. Lei, M. R. Lukatskaya, J. Park, Z. Huang, M. Lee, L. Shaw, S. Chen, A. A.
497 Yakovenko, A. Kulkarni, J. Xiao, K. Fredrickson, J. B. Tok, X. Zou, Y. Cui and Z. Bao, *Nat.*
498 *Energy*, 2018, **3**, 30–36.
- 499 23. S. Gu, Z. Bai, S. Majumder, B. Huang and G. Chen, *J. Power Sources*, 2019, **429**, 22–29.
- 500 24. D. Cai, M. Lu, L. Li, J. Cao, D. Chen, H. Tu, J. Li and W. Han, *Small*, 2019, **15**, 1902605.
- 501 25. F. Li, X. Zhang, X. Liu and M. Zhao, *ACS Appl. Mater. Interfaces*, 2018, **10**, 15012–15020.
- 502 26. S. Dong, L. Wu, M. Xue, Z. Li, D. Xiao, C. Xu, L. Shen and X. Zhang, *ACS Appl. Energy*
503 *Mater.*, 2021, **4**, 1568–1574.
- 504 27. D. Sheberla, J. C. Bachman, J. S. Elias, C. J. Sun, Y. Shao-Horn and M. Dincă, *Nat.*
505 *Mater.*, 2017, **16**, 220–224.
- 506 28. W. H. Li, K. Ding, H. R. Tian, M. S. Yao, B. Nath, W. H. Deng, Y. Wang and G. Xu, *Adv.*
507 *Funct. Mater.*, 2017, **27**, 1702067

- 508 29. X. Du, J. Zhang, H. Wang, Z. Huang, A. Guo, L. Zhao, Y. Niu, X. Li, B. Wu and Y. Liu,
509 *Mater. Chem. Front.*, 2020, **4**, 243–251.
- 510 30. B. Hoppe, K. D. J. Hindricks, D. P. Warwas, H. A. Schulze, A. Mohmeyer, T. J. Pinkvos,
511 S. Zailskas, M. R. Krey, C. Belke, S. König, M. Fröba, R. J. Haug and P. Behrens,
512 *CrystEngComm*, 2018, **20**, 6458–6471.
- 513 31. R. W. Day, D. K. Bediako, M. Rezaee, L. R. Parent, G. Skorupskii, M. Q. Arguilla, C. H.
514 Hendon, I. Stassen, N. C. Gianneschi, P. Kim and M. Dincă, *ACS Cent. Sci.*, 2019, **5**,
515 1959–1964.
- 516 32. J. W. M. Osterrieth, J. Rampersad, D. Madden, N. Rampal, L. Skoric, B. Connolly, M. D.
517 Allendorf, V. Stavila, J. L. Snider, R. Ameloot, J. Marreiros, C. Ania, D. Azevedo, E.
518 Vilarrasa-Garcia, B. F. Santos, X.-H. Bu, X. Zang, H. Bunzen, N. R. Champness, S. L.
519 Griffin, B. Chen, R.-B. Lin, B. Coasne, S. Cohen, J. C. Moreton, Y. J. Colon, L. Chen, R.
520 Clowes, F.-X. Coudert, Y. Cui, B. Hou, D. M. D, P. W. Doheny, M. Dincă, C. Sun, C.
521 Doonan, M. Thomas Huxley, J. D. Evans, P. Falcaro, R. Ricco, O. Farha, K. B. Idrees, T.
522 Islamoglu, P. Feng, H. Yang, R. S. Forgan, D. Bara, S. Furukawa, E. Sanchez, J. Gascon,
523 S. Telalovic, S. K. Ghosh, S. Mukherjee, M. R. Hill, M. Munir Sadiq, P. Horcajada, P.
524 Salcedo-Abraira, K. Kaneko, R. Kukobat, J. Kenvin, S. Keskin, S. Kitagawa, K. Otake, R.
525 P. Lively, S. J. A DeWitt, P. Llewellyn, B. v Lotsch, S. T. Emmerling, A. M. Pütz, C. Martí-
526 Gastaldo, N. M. Padial, J. García-Martínez, N. Linares, D. Maspoch, J. A. Suárez del Pino,
527 P. Moghadam, R. Oktavian, R. E. Morris, P. S. Wheatley, J. Navarro, C. Petit, D. Danaci,
528 M. J. Rosseinsky, A. P. Katsoulidis, M. Schröder, X. Han, S. Yang, M. A. van der Veen,
529 D. Rega, V. van Speybroeck, S. M. J Rogge, A. Lamaire, K. S. Walton, L. W. Bingel, S.
530 Wuttke, J. Andreo, O. Yaghi, B. Zhang, C. T. Yavuz, T. S. Nguyen, F. Zamora, C. Montoro,
531 H. Zhou, A. Kirchon and D. Fairen-Jimenez, *ChemRxiv*, 2021,
532 <https://doi.org/10.26434/chemrxiv.14291644.v1>.
- 533 33. S. Bi, H. Banda, M. Chen, L. Niu, M. Chen, T. Wu, J. Wang, R. Wang, J. Feng, T. Chen,
534 M. Dincă, A. A. Kornyshev and G. Feng, *Nat. Mater.*, 2020, **19**, 552–558.
- 535 34. Y. Misumi, A. Yamaguchi, Z. Zhang, T. Matsushita, N. Wada, M. Tsuchiizu and K. Awaga,
536 *J. Am. Chem. Soc.*, 2020, **142**, 16513–16517.
- 537 35. L. Mendecki and K. A. Mirica, *ACS Appl. Mater. Interfaces*, 2018, **10**, 19248–19257.
- 538 36. V. Rubio-Giménez, M. Galbiati, J. Castells-Gil, N. Almora-Barrios, J. Navarro-Sánchez, G.
539 Escorcia-Ariza, M. Mattera, T. Arnold, J. Rawle, S. Tatay, E. Coronado and C. Martí-
540 Gastaldo, *Adv. Mater.*, 2018, **30**, 1704291.

- 541 37. B. Dyatkin, V. Presser, M. Heon, M. R. Lukatskaya, M. Beidaghi and Y. Gogotsi,
542 *ChemSusChem*, 2013, **6**, 2269–2280.
- 543 38. T. Eguchi, D. Tashima, M. Fukuma and S. Kumagai, *J. Clean. Prod.*, 2020, **259**, 120822.
- 544 39. T. Chen, J. H. Dou, L. Yang, C. Sun, N. J. Libretto, G. Skorupskii, J. T. Miller and M. Dincă,
545 *J. Am. Chem. Soc.*, 2020, **142**, 12367–12373.
- 546 40. D. Bhattacharjya, D. Carriazo, J. Ajuria and A. Villaverde, *J. Power Sources*, 2019, **439**,
547 227106.
- 548 41. R. Iqbal, M. Q. Sultan, S. Hussain, M. Hamza, A. Tariq, M. B. Akbar, Y. Ma and L. Zhi,
549 *Adv. Mater. Technol.*, 2021, **6**, 2000941.
- 550 42. B. H. Toby and R. B. von Dreele, *J. App. Crystallogr.*, 2013, **46**, 544–549.
- 551 43. D. A. Gómez-Gualdrón, P. Z. Moghadam, J. T. Hupp, O. K. Farha and R. Q. Snurr, *J. Am.*
552 *Chem. Soc.*, 2016, **138**, 215–224.
- 553 44. R. Vicentini, L. M. da Silva, E. P. Cecilio, T. A. Alves, W. G. Nunes and H. Zanin,
554 *Molecules*, 2019, **24**, 1452.
- 555 45. B. Ravel and M. Newville, *J. Synchrotron Radiat.*, 2005, **12**, 537–541.
- 556 46. J. J. Rehr, J. J. Kas, F. D. Vila, M. P. Prange and K. Jorissen, *Phy. Chem. Chem. Phys.*,
557 2010, **12**, 5503–5513.
- 558 47. J. J. Rehr, J. J. Kas, M. P. Prange, A. P. Sorini, Y. Takimoto and F. Vila, *C. R. Phys.*, 2009,
559 **10**, 548–559.
- 560